NANO · MICRO small
www.small-journal.com

Organic Nano-Junctions: Linking Nanomorphology and Charge Transport in Organic Semiconductor Nanoparticles for Organic Photovoltaic Devices

*Hugo Laval, Yue Tian, Virginia Lafranconi, Matthew Barr, Paul Dastoor, Matthew M. Marcus, Guillaume Wantz, Natalie P. Holmes, Kazuhiko Hirakawa, and Sylvain Chambon**

In this study, innovative nanoscale devices are developed to investigate the charge transport in organic semiconductor nanoparticles. Using different steps of lithography techniques and dielectrophoresis, planar organic nano-junctions are fabricated from which hole mobilities are extracted in a space charge-limited current regime. Subsequently, these devices are used to investigate the impact of the composition and morphology of organic semiconductor nanoparticles on the charge mobilities. Pure donor nanoparticles and composite donor:acceptor nanoparticles with different donor compositions in their shell are inserted in the nanogap electrode to form the nano-junctions. The results highlight that the hole mobilities in the composite nanoparticles decrease by two-fold compared to pure donor nanoparticles. However, no significant change between the two kinds of composite nanoparticle morphologies is observed, indicating that conduction pathways for the holes are as efficient for donor proportion in the shell from 40% to 60%. Organic photovoltaic (OPV) devices are fabricated from water-based colloidal inks containing the two composite nanoparticles (P3HT:eh-IDTBR and P3HT:o-IDTBR) and no significant change in the performances is observed in accordance with the mobility results. Through this study, the performance of OPV devices have been succesfully correlated to the transport properties of nanoparticles having different morphology via innovative nanoscale devices.

1. Introduction

The wide field of organic electronics gathers many promising technologies, and their interests keep rising year after year. In particular, thin film electronic devices, such as organic photovoltaics (OPV), organic light-emitting diodes, and organic field-effect transistors (OFETs) are extensively studied, with constant improvement in their performances.[1–3] These developments, even though they are mainly focusing on improving performances, are gradually targeting the lab-to-fab considerations. The well-established consideration is the use of wet-process fabrication instead of dry process as it presents low-cost techniques (e.g., ink-jet printing, roll-to-roll coating), and versatility in producing large-area and flexible devices.[4–6] Another important aspect of industrialization, is the sustainability of the process.[7,8] Especially, the use of toxic organic solvents for thin film processing of organic electronic devices remains an issue as it requires highly efficient ventilation systems and solvent-trapping

H. Laval, V. Lafranconi, G. Wantz, S. Chambon
Univ. Bordeaux
CNRS
Bordeaux INP
IMS
UMR 5218, Talence F-33400, France
E-mail: sylvain.chambon@u-bordeaux.fr

Y. Tian, K. Hirakawa
Institute of Industrial Science
The University of Tokyo
4-6-1 Komaba, Meguro-ku, Tokyo 153–8505, Japan

M. Barr, P. Dastoor
Centre for Organic Electronics
University of Newcastle
Callaghan, NSW 2308, Australia

M. M. Marcus
Advanced Light Source
Lawrence Berkeley National Laboratory
Berkeley, CA 94720, USA

N. P. Holmes
School of Aerospace, Mechanical and Mechatronic Engineering
The University of Sydney
Sydney, NSW 2006, Australia

The ORCID identification number(s) for the author(s) of this article can be found under https://doi.org/10.1002/smll.202404112

DOI: 10.1002/smll.202404112

equipment. Halogenated solvents such as chloroform, chlorobenzene, or dichlorobenzene are still commonly used when targeting optimal film fabrication. However, they present high toxicity for the human body and the environment. For OPV cells, less-harmful and more sustainable solvents, such as xylene or 2-methyltetrahydrofuran, are sometimes used but still present significant toxicity.[9] Concerning OFETs, a wide range of "green solvents" have been studied, such as dimethyl carbonate and anisole, allowing a better choice toward sustainability.[10] Nevertheless, real benign solvents are still needed and the use of water is perfectly matching that demand. This choice has been made for OFETs and showed reliable transistor behavior with comparable charge carrier mobilities obtained from their organic solvent-based counterparts.[11,12] In the OPV community, aqueous inks have also been used for developing water-based solar cells using aqueous dispersions to process the active layer.[13] In recent years, the progress in the use of colloidal inks prepared by mini-emulsion allowed us to get closer to the symbolic power conversion efficiency value of 10%[14] and even exceed it by using the nanoprecipitation method.[15,16] These recent studies highlighted that the nano-morphology of the particles has an important impact on the final device performances and that it is important to identify it. Indeed, the internal morphology of the nanoparticle (NP) will drive the final morphology of the film and, as a result, the final properties of the device. Consequently, in an effort to understand the link between the morphology of nanoparticles and their performances, it is crucial to explore charge transport in these nano-objects. Diverse strategies are employed to study electronic transport in organic semiconductors. The dominant one remains the characterization of charge carrier mobility. Among the experimental techniques used for this purpose; time-of-flight),[17] field-effect transistor configuration,[18] electron or hole-only devices[19] or Charge Extraction by Linearly Increasing Voltage [20] are the most widely spread. However, all these techniques explored not only the charge transport in the nanoparticle itself but also between the nanoparticles since the properties of thin films, i.e., nanoparticle assemblies, have been studied.

Therefore, in an effort to investigate the charge transport properties at the single nanoparticle scale, nanogap devices have been developed to probe the charge transport at the nanoparticle scale. Nanoscale devices were fabricated using clean-room technology, e-beam lithography, and photo-lithography. A diode configuration with a sub-micrometric gap of 100 nm was developed in order to characterize the waterborne organic semiconductor nanoparticles. Doing so, it allows us to get closer to the electronic properties of a single nanoparticle. Dielectrophoresis (DEP) has been used to insert nanoparticles in the nanogap. This technique has been widely used in biology to trap cells or proteins[21,22] and it can also be used to attract dielectric particles[23] as well as semiconductors[24] or metallic particles.[25] DEP force is created when a particle is submitted to an alternative electric field, which creates a polarization in the particle. Depending on the permittivity and conductivities of the medium and the object, the force can be attractive or repulsive. The final nanogap devices with nanoparticles trapped inside – planar organic nano-junctions – were analyzed using hole-only devices and mobilities were extracted in space charge limited current (SCLC) regime. Pure poly(3-hexylthiophene) (P3HT) nanoparticles and P3HT blended with two different rhodanine-benzothiadiazole-coupled indacenodithiophene acceptor molecules (eh-IDTBR and o-IDTBR) composite nanoparticles have been synthesized by mini-emulsion and their morphology has been studied using synchrotron-based scanning transmission X-ray microscopy (STXM). These nanoparticles, having different compositions and morphology were inserted in the nanogap device and their mobility was extracted. Such a comprehensive study allowed us to link the composition and morphology of the nanoparticle to understand its possible impact on the final device's performance.

2. Results and Discussion

2.1. Design of Nano-Gap Structure and Trapping of Nanoparticles

2.1.1. Lithography Process for Nanogap Structures

The nanogap structures have been built on silicon substrates with 230 nm thermally grown silicon oxide using clean-room techniques. First e-beam lithography was used to design the nanoscale gap between the two electrodes (See supporting information for experimental details). Two kinds of nanoscale structures have been designed: trapezoid-shaped electrodes with a length and width of 100 nm and rectangular-shaped electrodes with a nanogap length of 100 nm and a width of 10 µm. Titanium (10 nm) and gold (50 nm) were thermally evaporated to form the electrodes followed by a lift-off process. Then photolithography was used to create the contacts, followed by a second evaporation of Ti/Au electrode and a lift-off process. The workflow of the design of such nanoscale electrode is schematized in **Figure 1a** and the detailed experimental procedure is described in supplementary information. The resulting devices are shown in Figure 1b (photograph) and 1c for scanning electron microscopy (SEM) images.

2.1.2. Dielectrophoresis Force for Organic Semiconductor Nanoparticles Insertion in Nanogap Structures

After the fabrication of the nanogap channels, nanoparticles have been incorporated using the DEP technique. Commonly known for biological application and trapping proteins and other biological objects,[21] DEP can also be used to trap other kinds of nano-objects such as metallic or semi-conducting particles from a liquid containing the nanoparticles.[24,25] The process involves the

N. P. Holmes
The University of Sydney Nano Institute
Faculty of Science
University of Sydney
Sydney, NSW 2006, Australia
N. P. Holmes
Australian Centre for Microscopy and Microanalysis
The University of Sydney
Madsen Building F09, Sydney, NSW 2006, Australia
K. Hirakawa, S. Chambon
LIMMS/CNRS-IIS (IRL2820)
Institute of Industrial Science
The University of Tokyo
4-6-1 Komaba, Meguro-ku, Tokyo 153–8505, Japan

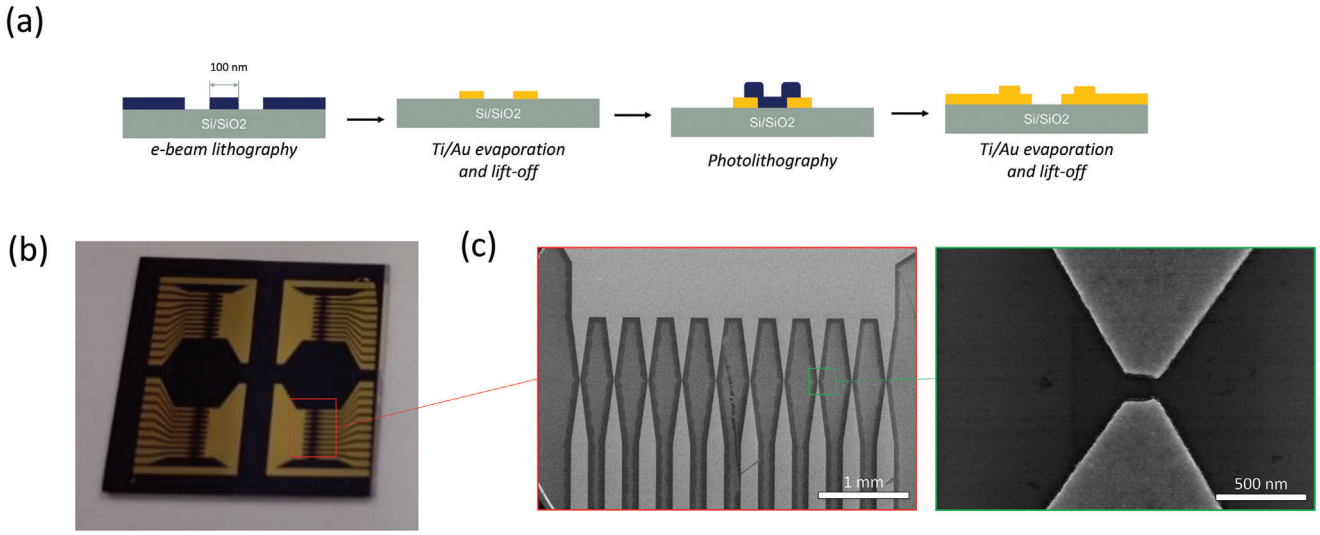

Figure 1. a) Workflow of the design of a nanoscale device for trapping organic semiconductor nanoparticles. Photograph b) and scanning electron microscopy c) images of the nanogap devices.

deposition of a drop of nanoparticle dispersion on the nanogap. Then an alternative voltage is applied between the two electrodes to induce the dielectrophoresis force. Finally, the excess water containing nanoparticles is removed and the substrate is dried. The dielectrophoresis force exerted to the nanoparticles depends a several parameters as described by the following Equation (1):

$$F_{DEP} = 2\pi\varepsilon_m a^3 Re[K(\omega)]\nabla E^2 \quad (1)$$

where a is the particle radius, ε_m is the permittivity of the suspending medium, E is the amplitude of the applied field (in case of AC field, root-mean-squared E), and $Re[K(\omega)]$ the real part of the Clausius-Mossotti factor (CM factor). The latter is dependent on the frequency of the applied alternative electric field and can be either positive or negative, which implies that the DEP force can be either positive or negative too. Re[K(ω)] is defined by the Equation (2):

$$Re[K(\omega)] = \frac{\left[(\varepsilon_p - \varepsilon_m)(\varepsilon_p + 2\varepsilon_m) + \frac{(\sigma_p - \sigma_m)(\sigma_p + 2\sigma_m)}{\omega^2}\right]}{\left[(\varepsilon_p + 2\varepsilon_m)^2 + \frac{(\sigma_p + 2\sigma_m)^2}{\omega^2}\right]} \quad (2)$$

where ε_p is the permittivity of the particle, σ_m is the conductivity of the suspending medium, σ_p is the conductivity of the particles, and ω is the angular frequency of the applied electric field.

The insertion of nanoparticles in trapezoid-shaped electrodes using DEP force was performed on P3HT nanoparticles synthesized by mini-emulsion (See experimental section for details) with 97 nm average diameter determined by DLS (Table S1, Supporting Information). The concentration of the dispersion was optimized to 0.05 mg mL^{-1} as well as some of the DEP conditions: the peak-to-peak voltage (V_{pp}) at 3 V and DEP time (t_{DEP}) equal to 5 s. The effect of the frequency of the electric field was studied. **Figure 2a** illustrates schematically the process of nanoparticle trapping. The real part of the Clausius-Mossotti factor was calculated for different frequency of the applied electric field considering that $\varepsilon_p = 2.9\ \varepsilon_0$,[26] $\varepsilon_m = 80\ \varepsilon_0$,[24] $\sigma_m = 4\ 10^{-4}$ S m^{-1}[24] and $\sigma_p = 10^{-3}$ S m^{-1}[27] (Figure 2b). The calculation shows that the DEP force can be either attractive or repulsive. At low frequencies, from 1 to 20 kHz, the DEP force is attractive and the CM factor constant. Starting from 20 kHz and for higher frequencies, the CM factor decreases until it reaches zero ≈170 kHz. For higher frequencies, the CM factor becomes negative and the DEP force turns repulsive. The impact of the frequency on the insertion of P3HT nanoparticles in trapezoid nanogaps is shown in Figure 2c. One can clearly see that for the low frequency of applied electric field, from 3 to 10 kHz, the trapping is highly efficient, with nanoparticles in the channel, as well as on the sides of the electrodes. For frequencies of 30 and 60 kHz, the nanoparticles are more directed to the nanogap and not around the electrodes, illustrating that the DEP force decreases while still being positive (attractive). However, starting from 100 kHz and up to 1 MHz, almost no NP is trapped in the channel, suggesting strongly that the DEP force became repulsive.

2.1.3. Application to P3HT Nanoparticles

In order to investigate the possibility of probing the charge transport using such nano-junction, P3HT NP has been trapped in nanogap, either in trapezoid geometry or with rectangular geometry. For trapezoid configuration, the DEP conditions were V_{pp} = 3 V, t_{DEP} = 5 s, and f = 60 kHz and for rectangular configuration, the same conditions were used except for V_{pp} which was set to 5 V. After the DEP step, the excess of water is removed and the substrates dried. The nanogap before and after DEP are presented in Figure S1 (Supporting Information).

Current-voltage (I–V) characterization of the trapezoid and rectangular nano-junctions was performed. Plotting the I–V curves in logarithmic scales allowed us to identify two regimes (**Figure 3**): a linear regime, attributed to the ohmic regime, and a quadratic regime, attributed to SCLC regime,[28,29] from

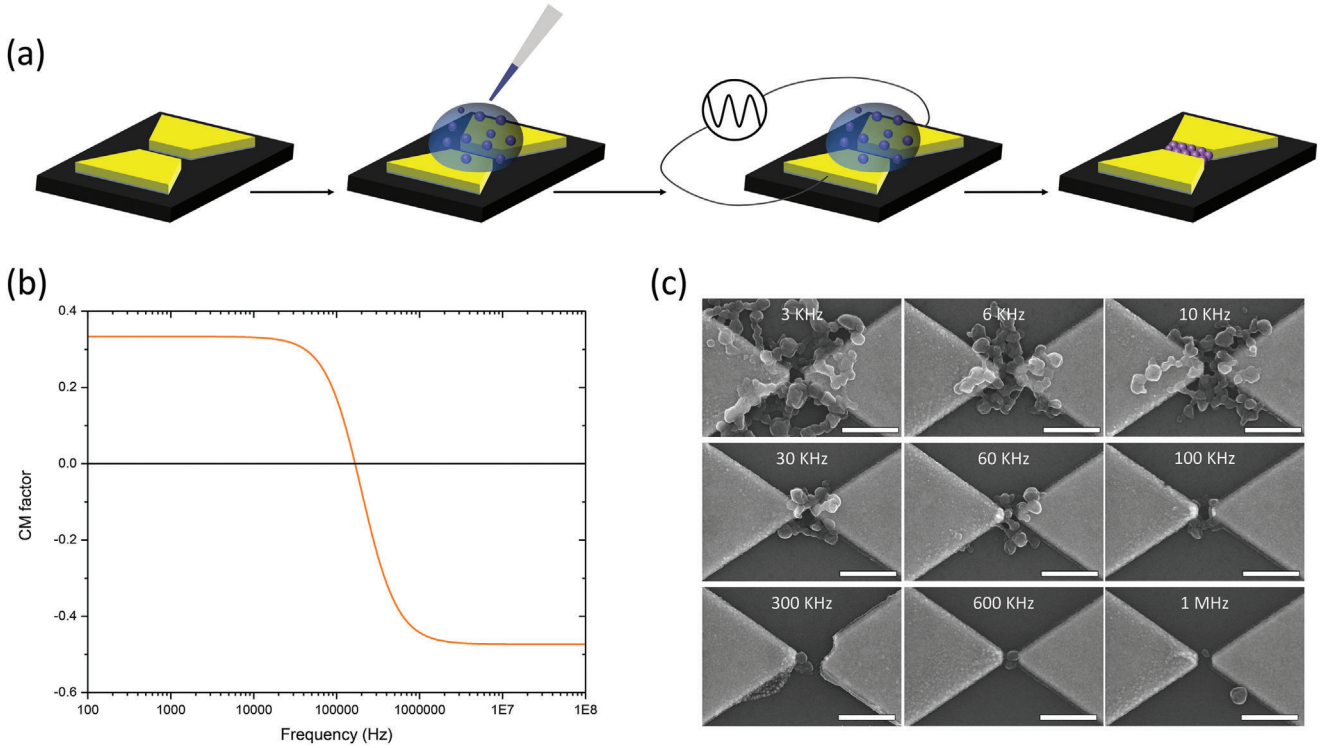

Figure 2. a) Different steps for the insertion of nanoparticles in the nanogap device. b) Calculation of the CM factor for the applied conditions. c) SEM images of the different nanogap after the DEP process and for various applied AC electric fields (scale bars: 500 nm).

which the charge mobility can be extracted according to the Mott-Gurney law:

$$J_{SCLC} = \frac{9}{8}\varepsilon_0\varepsilon_r\mu\frac{V^2}{L^3} \quad (3)$$

In which ε_r is the relative permittivity of the organic semiconductor, μ the charge carrier mobility (in our case the hole mobility μ_{h+}), and L is the distance between the two electrodes. The current density, J, was calculated using the section of the electrode as area: $A = W \times e$, with W and e as the width and the thickness of the electrodes.

From the SCLC regime, hole mobilities were extracted for the rectangular and trapezoid geometries, 4.8 and 5.3 10^{-4} cm^2 V^{-1} s^{-1} respectively (in forward bias), a value commonly found for P3HT.[30] However, for the trapezoid configuration, a perfectly quadratic regime was not found, and only slopes ≈1.63 were extracted, indicating that the space charge-limited current regime might not have been reached for this structure. As one can see in Figure 2c (60 kHz) and Figure S1d

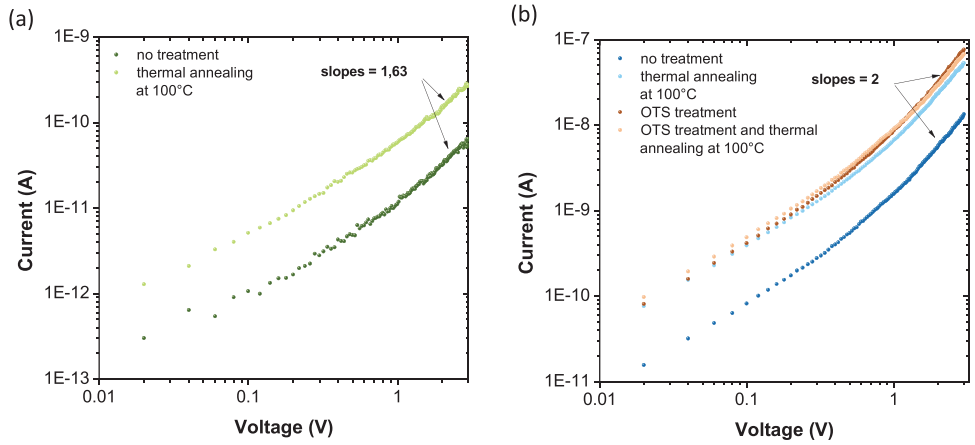

Figure 3. Current–voltage characterization plotted in logarithmic scale of the trapezoid a) and rectangular b) organic nano-junctions for different treatments applied (thermal annealing, OTS treatment).

Table 1. Hole mobilities (μ_{h+}) in $cm^2\ V^{-1}\ s^{-1}$ for various nanogap device configurations (trapezoid and rectangular) and different treatments (thermal annealing, OTS treatment). ($n = 4 - 7$).

Architecture	OTS treatment	Thermal treatment	μ_{h+} [$cm^2\ V^{-1}\ s^{-1}$]		Error [$cm^2\ V^{-1}\ s^{-1}$]	
			forward	reverse	forward	reverse
Trapezoid	no	no	4.3×10^{-4}	5.3×10^{-4}	$\pm 3.7 \times 10^{-4}$	$\pm 2.0 \times 10^{-4}$
		yes	2.7×10^{-3}	3.8×10^{-3}	$\pm 1.5 \times 10^{-3}$	$\pm 1.0 \times 10^{-3}$
Rectangular	no	no	4.8×10^{-4}	5.0×10^{-4}	$\pm 1.2 \times 10^{-4}$	$\pm 1.4 \times 10^{-4}$
		yes	2.3×10^{-3}	2.4×10^{-3}	$\pm 0.7 \times 10^{-3}$	$\pm 0.8 \times 10^{-3}$
	yes	no	2.4×10^{-3}	2.6×10^{-3}	$\pm 0.7 \times 10^{-3}$	$\pm 0.8 \times 10^{-3}$
		yes	2.4×10^{-3}	2.9×10^{-3}	$\pm 0.4 \times 10^{-3}$	$\pm 0.6 \times 10^{-3}$

(Supporting Information), nanoparticles are not only present inside the 100 nm gap but also around. In these side parallel pathways for charges, the SCLC regime might not have been reached, resulting in *I–V* characteristic not purely quadratic. In addition, the error calculated for the trapezoid structure is large, on the order of magnitude as the mobility itself (**Table 1**). Therefore, mobility extracted from such devices is not fully reliable. On the other hand, for the rectangular nanostructure, a slope of two could be found in all cases, a strong indication that the space charge limited current regime is reached. The error calculated on the mobility values for the rectangular configuration is lower than that of the trapezoid configuration, especially for devices submitted to octadecyltrichlorosilane (OTS) treatment or thermal annealing, making them reliable. For these reasons, nanogap devices with large width (W) are used in the following part of the study.

In the second step, several steps of optimization were performed on rectangular-shaped nano-devices. First, the effect of thermal annealing was investigated, and the devices were submitted to 100 °C for 10 min. The mobility extracted using the SCLC regime increased by one order of magnitude, up to 2.3 10^{-3} $cm^2\ V^{-1}\ s^{-1}$ (in forward bias), suggesting improved contact between the nanoparticles and the electrodes. Then, the effect of OTS treatment of the substrate was studied. OTS is commonly used in OFET to passivate the oxide surface and remove possible charge traps.[31] Such treatment was investigated in a rectangular configuration, with and without thermal treatment. The extracted mobility is presented in Table 1 and shows that, with the OTS treatment, the nano-gap devices present an optimal hole mobility of 2.4 10^{-3} $cm^2\ V^{-1}\ s^{-1}$ similar to those which were submitted only to thermal annealing 2.3 10^{-3} $cm^2\ V^{-1}\ s^{-1}$. These results suggest that both treatments (OTS treatment and thermal treatment) have a similar effect. One can suggest that both treatments lead to the improvement of charge transport between particles and/or between the particle and the electrode by improving the contact between nanoparticles and/or the electrodes. This effect can be explained since OTS treatment can get rid of morphological trap,[32] herein represented by interparticle spacing, grain boundaries or poor contact with the electrode, as the treatment can lead to better uniformity in the channel. On the other hand, thermal annealing of P3HT nanoparticles on OTS-treated substrates does not improve the mobility further, reaching also 2.4 10^{-3} $cm^2\ V^{-1}\ s^{-1}$. This result is surprising as thermal annealing can improve the hole mobilities in P3HT thin films deposited from organic solvent due to enhanced crystallinity.[33] This difference between P3HT thin films deposited from organic solvents and P3HT nanoparticles can be explained by the fabrication method of the nanoparticles (mini-emulsion) which involves a thermal treatment for several hours and can enhance the crystallinity of P3HT in the NP. UV–visible spectra of P3HT thin films fabricated from nanoparticles before and after thermal treatment have been recorded (Figure S2, Supporting Information). One can clearly see the two vibronic peaks of P3HT at 554 and 604 nm – an indication of the crystallinity of P3HT – already at room temperature (without thermal treatment). The thermal annealing at 130 °C did not lead to a significant change in the position or intensity of these peaks, indicating that the crystallinity has not been improved. This result is in accordance with the absence of improvement of hole mobility upon thermal annealing at 100 °C. These first experiments on pure P3HT allowed us to identify the conditions for fabrication of the nano-junctions (OTS treatment, 100 °C thermal annealing) which will be used in the following part of the study.

2.2. Investigation on Composite Donor:Acceptor of P3HT:o-IDTBR and P3HT:eh-IDTBR Nanoparticles: Impact of the Morphology

In a previous work, the morphology of different donor/acceptor composite nanoparticles has been investigated and the different studies have shown that a core-shell-like morphology is often observed with the higher surface energy material of the two materials preferentially migrating in the nanoparticle core, and the lower surface energy material to the nanoparticle shell.[34] This result was particularly clear with two similar systems, P3HT:eh-IDTBR and P3HT:o-IDTBR, where the donor material P3HT is respectively predominantly located in the core and in the shell (**Figure 4**). In order to investigate the impact of the morphology and the change in the spatial distribution of the donor material (P3HT) in the particle on the hole mobility of composites donor/acceptor particles, the nanogap structures previously developed have been used.

2.2.1. Morphology Investigation

Composite donor/acceptor nanoparticles with the two systems described earlier, P3HT:eh-IDTBR and P3HT:o-IDTBR, have

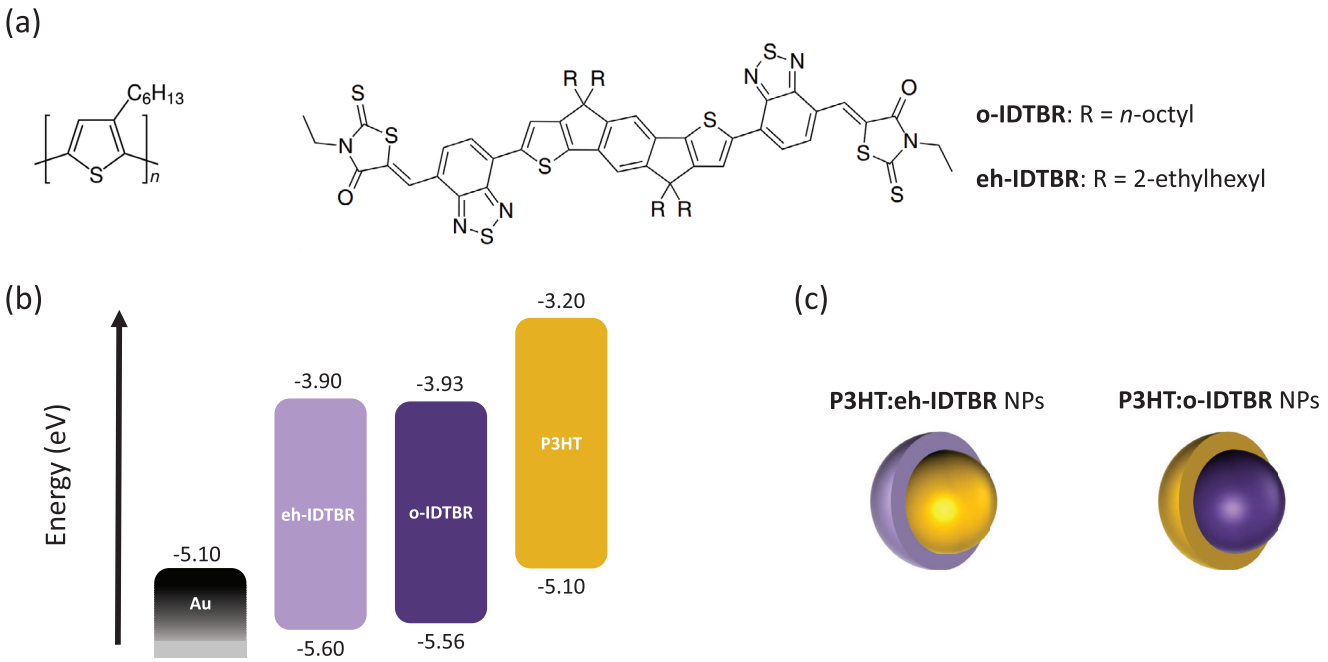

Figure 4. a) Chemical structure of donor material P3HT and acceptor materials o-IDTBR and eh-IDTBR, b) Energy level diagram of eh-IDTBR, P3HT and o-IDTBR and gold electrode, c) Schematic representation of P3HT:eh-IDTBR NPs and P3HT:o-IDTBR NPs internal morphology.

been synthesized. Prior to the investigation of the charge transport, the internal morphology for each system was revealed using scanning transmission X-ray microscopy (STXM) at beamline 5.3.2.2 at the Advanced Light Source (ALS) synchrotron, as a powerful tool for determining the composition of organic blends in thin film as well as in nanoparticles.

STXM images and the extracted radial profile (**Figures 5** and **6**) show the distribution of each material inside the nanoparticle. A core-shell model is applied to extract the true core composition based on the measured nanoparticle center composition and the core-shell dimensions, as reported in our previous work.[35] For P3HT:o-IDTBR nanoparticles, the donor material is driven to the shell as it has a slightly lower surface energy than the o-IDTBR (26.9 and 28.1 mJ m^{-2} respectively).[34] In the case of the P3HT:eh-IDTBR, because of the higher surface energy of P3HT as compared to eh-IDTBR (26.9 and 18.3 mJ m^{-2} respectively),[34] the P3HT is mainly driven to the core of the nanoparticles. However, since the two non-fullerene acceptors (NFA) materials do not have high surface energy as compared to fullerene acceptors (i.e., $PC_{61}BM$ = 38.2 mJ m^{-2}; $PC_{71}BM$ = 39 mJ m^{-2}),[34] the compositions of shell and the core of the nanoparticles are more balanced than generally observed for fullerene-based particles: the proportions of P3HT in the shell are 40% and 60% for P3HT:eh-IDTBR and P3HT:o-IDTBR respectively. Therefore, it is possible to conclude that P3HT:eh-IDTBR NP has an acceptor-rich shell while P3HT:o-IDTBR has a donor-rich shell. Such a difference in the composition of the NP may have an impact on the charge mobility and more specifically on the hole transport through the P3HT. One can argue that a better pathway for holes is obtained with the P3HT:o-IDTBR nanoparticle as the P3HT is mainly in the shell, whereas poor pathways might confine charges inside the core of the P3HT:eh-IDTBR nanoparticle.

2.2.2. Mobility Studied through Nanogap Devices

To probe a possible impact of the P3HT spatial distribution in the nanoparticle on the hole mobility, the nano-gap device described earlier is used. The architecture was slightly improved in order to enhance the signal-to-noise ratio while keeping a geometrical ratio between channel length and width of at least 20 (W/L = 25 in our case). This factor is necessary to be able to probe the material in the channel and avoid artifacts coming from the edges that might induce an overestimation of the mobility.[36] The architecture used had L = 100 nm and W = 2.5 µm (Figure S3, Supporting Information). As shown in **Figure 7a**, different kinds of nanoparticles were successfully inserted in the nanogap channels: P3HT, P3HT:o-IDTBR, and P3HT:eh-IDTBR using optimized DEP conditions (V_{pp} = 5 V, f = 60 kHz, t_{DEP} = 5 sec).

As shown in the energy level diagram (Figure 4b), hole injection occurs from the Fermi level (E_F) of the gold electrode to the highest occupied molecular orbital (HOMO) of P3HT. The energy barrier between the E_F of the gold electrode and the HOMO of the two NFAs should be large enough to not be overcome even if they might present ambipolar transport.[37] To confirm these assumptions, and verify if the injection and the extraction of the holes is only happening through the P3HT, eh-IDTBR and o-IDTBR pure nanoparticles were inserted in the nano-gap devices as a control test. As a result, no current above the noise level was extracted (Figure S4, Supporting Information), confirming either the lack of hole injection through the two NFAs or their poor ability to transport holes.

In Figure 7b the current–voltage characteristics in logarithmic scales (log(I)–log (V)) of nanogap devices with either pure P3HT nanoparticles and the two blend nanoparticles (P3HT:o-IDTBR and P3HT:eh-IDTBR) are presented. One can observe from the log(I)-log(V) plots two distinct regimes. Similarly to what was

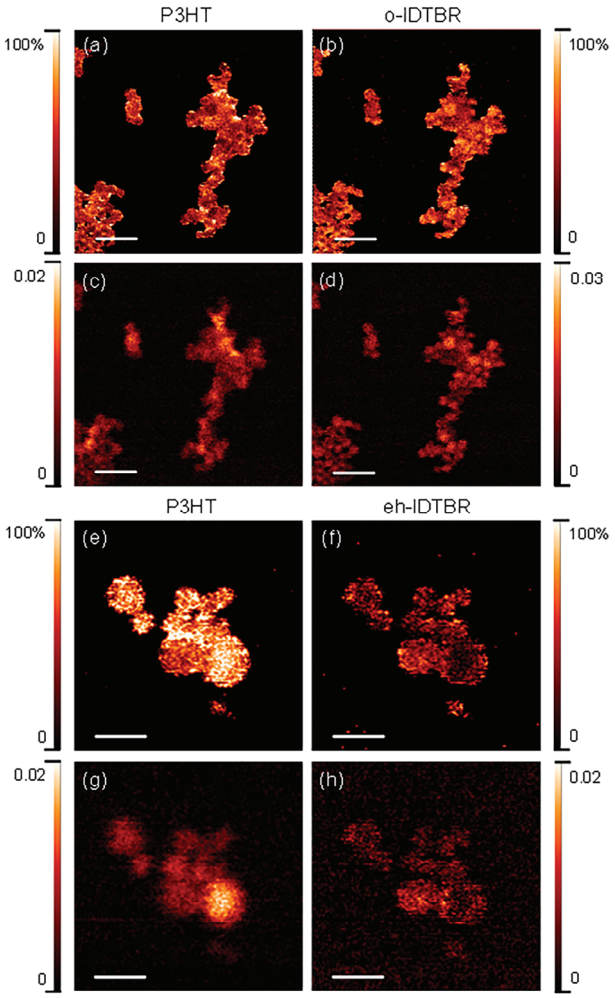

Figure 5. STXM fractional composition maps showing the concentration of a) P3HT and b) o-IDTBR with corresponding STXM mass plots c and d) for 1:1 P3HT:o-IDTBR nanoparticles; STXM fractional composition maps showing the concentration of e) P3HT and f) eh-IDTBR with corresponding STXM mass plots g and h) for 1:1 P3HT:eh-IDTBR nanoparticles. The scale bars in a – d are 1 µm, and the scale bars in e – h are 500 nm. The color contrast is scaled such that light colors correspond to higher component concentrations. For the mass plots (c, d, g, h) the color scale bars indicate the concentration of a component in mg cm^{-2}.

previously observed for trapezoid and rectangular electrodes, at a low electric field ($V \leq 0.2$ V) the first regime corresponds to the ohmic regime (slope of 1), thus confirming an ohmic injection and extraction for the holes, and ticking an important assumption for the use of the SCLC theory.[38] The second regime is seen at a higher electric field ($V \geq 1$ V) for each nanoparticle system and is associated with the SCLC regime where the current depends quadratically on the applied voltage (slope of 2) as described previously (See Figure S5, Supporting Information for the different fits).

From these plots, a notably higher current for the pure P3HT nanoparticles is observed compared to the two composite nanoparticles. Such a difference in hole transport can be explained by various factors such as the purity of each phase, the crystalline behavior, and the transport mechanisms.[39,40] From this first analysis, blending P3HT with either IDTBR acceptors seems to disturb the transport of the holes within the nanoparticle compared to what happens in a pure P3HT nanoparticle. The hole mobility was estimated from the SCLC regime identified on the I-V characteristics and extracted for several devices. The results are presented in **Table 2** and Figure S6 (Supporting Information).

Table 2. Summary of the μ_{h+} for P3HT NPs, P3HT:o-IDTBR NPs and P3HT:eh-IDTBR NPs ($n = 3$).

Nanoparticle system	μ_{h+} [cm^2 V^{-1} s^{-1}]		error [cm^2 V^{-1} s^{-1}]	
	forward	reverse	forward	reverse
P3HT	4.5×10^{-3}	4.4×10^{-3}	$\pm 1.2 \times 10^{-3}$	$\pm 0.6 \times 10^{-3}$
P3HT:o-IDTBR	2.3×10^{-3}	2.6×10^{-3}	$\pm 0.4 \times 10^{-3}$	$\pm 0.2 \times 10^{-3}$
P3HT:eh-IDTBR	1.2×10^{-3}	1.5×10^{-3}	$\pm 0.2 \times 10^{-3}$	$\pm 0.4 \times 10^{-3}$

For P3HT:eh-IDTBR and P3HT:o-IDTBR, a hole mobility (forward bias) of 1.2 ± 0.4 10^{-3} cm^2 V^{-1} s^{-1} and 2.3 ± 0.2 10^{-3} cm^2 V^{-1} s^{-1} respectively was calculated, whereas a hole mobility of 4.5 ± 1.2 10^{-3} cm^2 V^{-1} s^{-1} is obtained for pure P3HT NPs. These results first confirm that the addition of the acceptor slightly disturbs the hole transport through in the composite nanoparticles, the mobility decreasing by half compared to pure P3HT NP. In addition, this analysis can help understand the possible impact on the hole mobility induced by a change of polymer content in the shell of the composite nanoparticles. However, only a very slight increase in the hole mobility in forward bias is observed for P3HT:o-IDTBR nanoparticles compared to P3HT:eh-IDTBR nanoparticles. Considering also the error calculated on the mobilities, these results suggest that the NP morphology and the P3HT content in the shell (60% in P3HT:o-IDTBR NPs / 40% in P3HT:eh-IDTBR NPs) have no significant impact on the hole mobilities in P3HT:IDTBR composite nanoparticles. Even a limited amount of P3HT in the shell (here 40% for P3HT:eh-IDTBR NPs) is enough to transport holes efficiently through the nanoparticle.

2.2.3. Organic Photovoltaic Devices from P3HT:IDTBR Nanoparticles

Photovoltaic devices incorporating P3HT:eh-IDTBR and P3HT:o-IDTBR composite nanoparticles from water-based inks have been fabricated using standard inverted architecture (Glass/ITO/ZnO/active layer/MoO_3/Ag) and characterized under dark and 1-sun illumination.

For the devices fabricated from water-based inks, the effect of the thermal annealing temperature on the NP-based active layer was first investigated and an optimal thermal annealing temperature was found at 130 °C (Table S2, Supporting Information). Modest performances were obtained with power conversion efficiencies (PCE) of 1.44% and 1.62% for devices with P3HT:o-IDTBR and P3HT:eh-IDTBR respectively. Increasing the thermal annealing temperature to 150 °C led to a decrease in the performances of the devices down to 1.05% for P3HT:o-IDTBR. It has been shown that when nanoparticles are synthesized by miniemulsion technique, the thermal annealing temperature necessary to achieve the nanoparticles' sintering and reach optimal

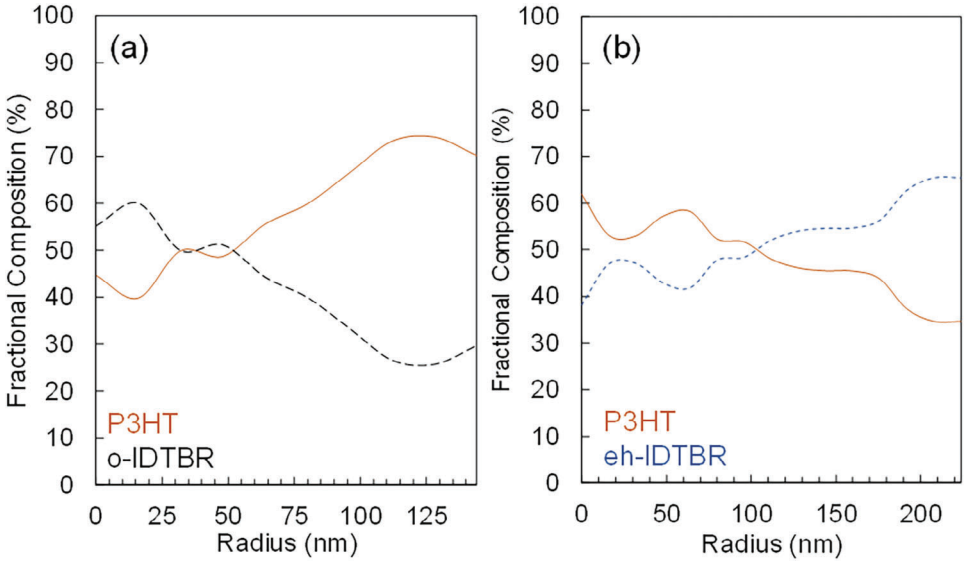

Figure 6. Radial composition profiles extracted from STXM maps of representative nanoparticles for a) P3HT:o-IDTBR and (b) P3HT:eh-IDTBR. Composition of P3HT (orange), o-IDTBR (black dashed), eh-IDTBR (blue dotted).

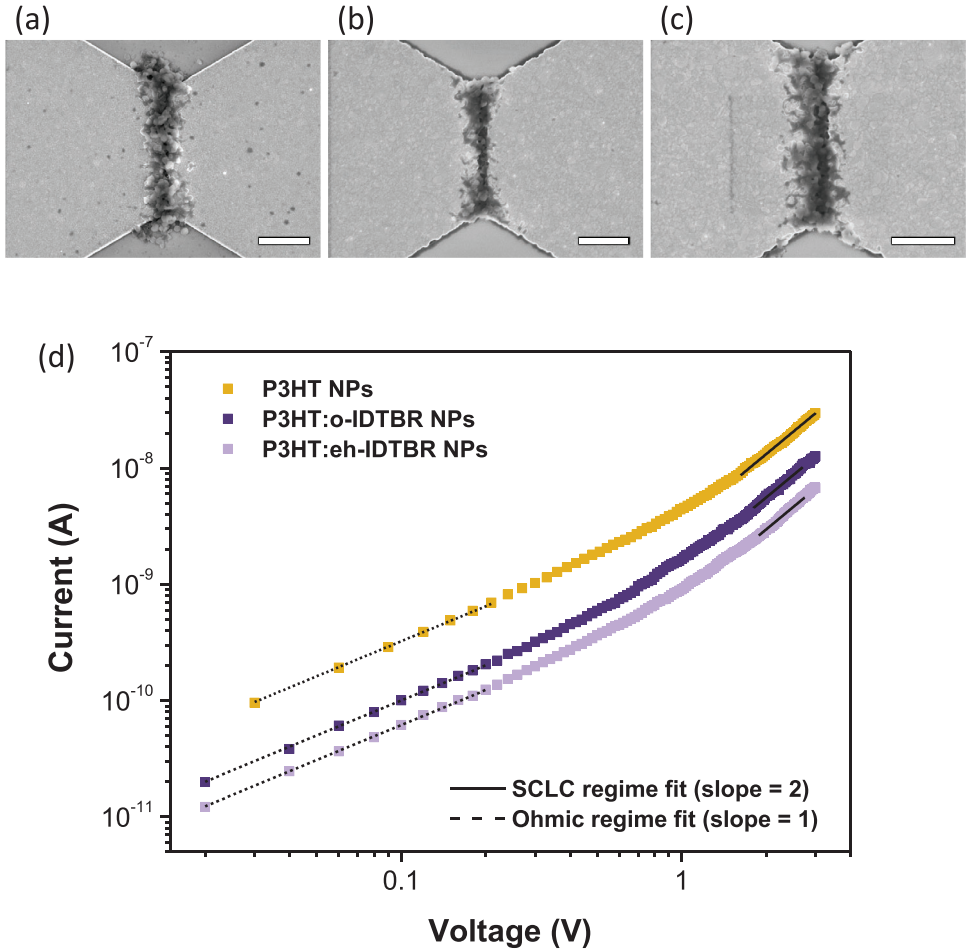

Figure 7. SEM images of the nanogap device with L = 100 nm and W = 2.5 µm after the dielectrophoresis step and filled with a) P3HT NPs, b) P3HT:eh-IDTBR NPs, and c) P3HT:o-IDTBR NPs (scale bars: 1 µm). d) Current–voltage characteristics plotted in logarithmic scales of P3HT NPs (orange), P3HT:o-IDTBR NPs (dark purple), and P3HT:eh-IDTBR NPs (light purple) with their ohmic region fit (black dashed line) and SCLC region fit (black line).

Table 3. Short-circuit current density (J_{sc}), open-circuit voltage (V_{oc}), fill factor (FF), and power conversion efficiency (PCE) of organic photovoltaic devices with P3HT:o-IDTBR and P3HT:eh-IDTBR as active layer prepared from water-based nanoparticles dispersions or organic solvents. ($n = 8$).

	J_{sc} [mA/cm^2]	V_{oc} [V]	FF	PCE [%]
P3HT:o-IDTBR NP (water)	7.90 ± 0.17	0.43 ± 0.01	0.55 ± 0.01	1.86 ± 0.10
P3HT:o-IDTBR (organic)	13.19 ± 0.15	0.71 ± 0.01	0.62 ± 0.05	5.8 ± 0.40
P3HT:eh-IDTBR NP (water)	6.43 ± 0.17	0.46 ± 0.01	0.55 ± 0.02	1.62 ± 0.27
P3HT:eh-IDTBR (organic)	11.17 ± 0.76	0.72 ± 0.02	0.53 ± 0.03	4.21 ± 0.19

performances can be quite high, up to 200 °C. However, concomitantly, phase segregation between the donor and the acceptor phase can also occur at such high temperatures. One can suggest that for P3HT:IDTBR nanoparticles-based active layer, a thermal annealing temperature of 130 °C is not enough to efficiently sinter the nanoparticle but a temperature above 130 °C promotes large phase segregation leading to a drop in efficiency. In addition, two different nanoparticle diameters have been synthesized to assess their impact on the water-based OPV devices. Small nanoparticles with a diameter of ≈53 nm and larger ones of 74 nm have been made for the two composite nanoparticles (Figure S7 and Table S1, Supporting Information). For each system, having smaller nanoparticles enhanced the performances with a significant increase of open-circuit voltage (V_{oc}) and fill factor (FF) (Figure S8 and Table S3, Supporting Information). Interestingly, this is even more evident for P3HT:o-IDTBR nanoparticles. The NFA in the latter system shows high crystallinity upon thermal annealing. Decreasing the nanoparticle size of P3HT:o-IDTBR is suspected to weaken the high crystallinity of o-IDTBR,[41] which can positively impact the V_{oc} and FF.[42] With such kind of NP size optimization, optimal performances up to 1.86% PCE were achieved for P3HT:o-IDTBR OPV devices fabricated from water-based colloidal inks. The optimized photovoltaic parameters for the different systems (P3HT:o-IDTBR and P3HT:eh-IDTBR) are summarized in **Table 3**. Control devices fabricated from organic solvent have also been prepared as a comparison (Figure S9, Supporting Information).

The devices fabricated from water suffer from very low V_{oc} compared to the reference fabricated from organic solvent, with a loss of 260 to 280 mV. A possible explanation for the large difference in V_{oc} could be the higher crystallinity of the acceptor and/or the donor in the case of nanoparticle-based thin films. UV–visible absorbance spectra of P3HT:eh-IDTBR and P3HT:o-IDTBR films deposited with chloroform and water are shown in Figure S10 (Supporting Information). The thin film made of nanoparticles presents sharper and more intense red-shifted vibronic peaks which could indicate higher crystallinity of both the donor and the acceptor, compared to that of thin film processed from organic solvent. The formation of large crystalline domains of either donor or acceptor has already been shown to decrease the energy of the charge transfer state (E_{CT}) and, as a consequence, the V_{oc}. Decreases of 100 to 150 mV of the V_{oc} have been reported upon crystallization of phenyl- C_{61}-butyric acid methyl ester (PCBM)[43] and P3HT[44] respectively. Another explanation might come from the difference of crystallization between the donor and the acceptor which was found to increase the non-radiative energy loss ($\Delta V_{oc}^{non\text{-}rad}$) and thus reduce the V_{oc}.[45,46] In particular, the latter mechanism has been observed when increasing the crystallinity of o-IDTBR with respect to that of the donor material, thus reducing the V_{oc} of 100 mV due to non-radiative recombination. The strong aggregation of the donor and/or the acceptor could result in a strong decrease of the E_{CT} or an increase of $\Delta V_{oc}^{non\text{-}rad}$, and as a consequence, explain the drop of 260–280 mV in V_{oc}. More investigations are ongoing to confirm (or disprove) these hypotheses and gain an understanding of the V_{oc} loss in water-processed OPV devices.

In addition, we compared our results with the literature, Xie et al. fabricated OPV devices based on P3HT:o-IDTBR nanoparticles prepared by mini-emulsion. These researchers reported higher performances, with 2.53% PCE.[47] The lower PCE obtained in our study is mainly due to a significant decrease of the V_{oc}, 430 mV for this study compared to 750 mV reported by Xie et al. Several hypotheses could explain such discrepancy. Indeed, it has been shown that the P3HT molar mass can impact the V_{oc} of P3HT-based nanoparticles OPV devices.[48] Moreover, as mentioned before, higher crystallinity of either P3HT or IDTBR molecules could also be the reason for such a decrease, as an aggregation of donor and/or acceptor has been shown to lead to V_{oc} losses.[42–44]

Nevertheless, when comparing P3HT:eh-IDTBR and P3HT:o-IDTBR devices prepared for water-based nanoparticle dispersions annealed at 130 °C, no significant difference is observed in the performances of the devices, with 1.62% and 1.86% PCE respectively. In particular, the fill factor, particularly sensitive to charge transport, is identical for both kinds of active layer: 0.55 for P3HT:eh-IDTBR and P3HT:o-IDTBR. Such result can be related to the hole mobilities obtained using nanogap devices in which no significant difference in hole transport has been observed between the two kinds of particles, 1.2 and 2.3 10^{-3} cm^2 V^{-1} s^{-1} for P3HT:eh-IDTBR and P3HT:o-IDTBR NP respectively.

3. Conclusion

Devices with nanogap electrodes have been developed in which either pure donor NP (P3HT) or composite NP (P3HT:eh-IDTBR and P3HT:o-IDTBR) have been inserted using the dielectrophoresis technique. It resulted in planar organic nanojunctions, from which we managed to extract hole mobilities. The analysis showed that the hole mobility in composite P3HT:IDTBR nanoparticles decreases by a factor of two compared to pure P3HT NP. However, no significant difference was observed between the two kinds of composite nanoparticles (P3HT:eh-IDTBR and P3HT:o-IDTBR) although the proportion of P3HT in their shell was different. It suggests that conduction pathways for the positive charges could be efficiently found even for a proportion as low as 40%. Such similarity in the charge transport at the nanoscale could also be observed on OPV devices with active layers made of either P3HT:eh-IDTBR and P3HT:o-IDTBR NP (from water-based inks). Indeed, similar photovoltaic performances were measured in both cases with 1.62% and 1.86% PCE respectively. To conclude, this study helped to create a link between the performances of macro-scale devices (OPV devices) and the properties at the nanoscale of organic semiconductor nanoparticles. This development also opens the route to widen the understanding of the nanoscale properties of organic

semiconductor nanoparticles using nanoscale devices such as organic nano-junctions.

4. Experimental Section

Materials: Chloroform (≥99%), sodium dodecyl sulfate (SDS), and trichloro(octadecyl)silane were purchased from Sigma Aldrich. Deionized water was obtained from a PURELAB Flex system (≈15 MΩ). Poly(3-hexylthiophene) (P3HT) (M_w = 53 kDa) was purchased from Solaris Chem Inc. o-IDTBR and eh-IDTBR was purchased from 1-Material. All the materials were used as received without further purification.

Nanoparticles Synthesis: Water-based inks were obtained with mini-emulsion synthesis. For the organic phase, a total of 20 mg mL^{-1} was first dissolved in active material (wt% of 1:1 for P3HT:o-IDTBR and P3HT:eh-IDTBR) mixture in chloroform stirred 2 h at 65 °C in a nitrogen-filled glovebox. Aqueous phase was obtained by dissolving 2 mg mL^{-1} of SDS in MilliQ water and stirred 30 min at RT. A macro-emulsion was then obtained by adding the organic phase into the aqueous phase with 1:5 volume ratio and stirring for 1 h at 40 °C (1000 rpm). The mini-emulsion dispersion was formed by sonicating the macro-emulsion using a BRANSON Digital Sonifier 450 in an ice-water bath for 2 min at 15% of the maximum power in an ice-water bath. Chloroform evaporation was completed by stirring the mini-emulsion 3 h at 65 °C. In order to eliminate the excess SDS, the centrifugal step was carried out by using an Amicon Ultra-15 centrifuge filter (cut-off 100 kDa) and a Hettich Universal 320 centrifugal. Three centrifugation cycles were done at 3500 rpm for 5 min. The retentate was raised to 15 mL with MilliQ water between each step. Final aqueous dispersions were obtained with a concentration of 0.05 mg mL^{-1} of active materials. The concentrations were kept like this needed for the trapping of the nanoparticles using the dielectrophoresis method.

Nanogap Electrodes Fabrication: The nano-gap electrodes were fabricated on Si/SiO_2 substrates. Prior to the deposition of the EBL resist, the substrates were cleaned by sequential ultrasonic treatments: acetone and isopropanol. Consecutively, the substrates were dried for 10 min at 110 °C in an oven containing Ar flow. A solution of PMMA in anisole (wt% 6) was spin-coated onto the substrate at 4000 rpm for 50 sec. PMMA resist film was then dried for 5 min at 180 °C in an oven containing Ar flow. Then, electron-beam lithography (JEOL JBX-6300SG) was used to transfer the pre-defined pattern of the nano-gap electrode onto the substrate, employing a current of 300pA and accelerating voltage of 100 kV. The dose value used in the writing process was 1100 μC cm^{-2}. Next, the samples were developed in MIBK:IPA (1:3) solution for 45 s, and then rinsed in IPA for 30 s, followed by drying in a N_2 flow. Metal deposition was carried out using e-beam evaporation of Ti/Au (10/50 nm, e = 60 nm). Subsequently, the lift-off for e-beam evaporated metal electrodes was performed in hot acetone followed by IPA rinsing and N_2 drying. In order to perform electrical characterization using a probe station, the nano-gap electrodes were extended by using photolithography and thermal evaporation of Ti/Au (10/50 nm) following the pattern in Figure 1.

Trapping of the Nanoparticles Using the DEP Force: Nanoparticles were trapped in the nano-gap using the dielectrophoresis force. A drop of 3 μL of the colloidal dispersion (0.05 mg mL^{-1}) was dispensed onto the nano-gap area. The AC (sinusoidal) signal was generated by an Agilent waveform generator 33521B. This step was performed in the dark and in the air. Finally, the remaining drop was removed by capillarity using an ultra-absorbent wipe.

Electrical Characterization of the Nano-Gap Devices: The nano-gap devices were measured in the dark and in the air under a probe station and using an Agilent B1500A semiconductor device parameter analyzer. Single voltage sweeps from −3 to +3 V were done to extract the *I–V* curves of each device.

Dynamic Light Scattering: Hydrodynamic diameters of the nanoparticles were determined by dynamic light scattering using a Zetasizer Nano ZS from Malvern Instruments at a detection angle of 173°. Autocorrelation curves were averaged from 10 to 15 acquisitions depending on the intensity of the scattered signal. The cumulants method was used to determine the Z-average hydrodynamic diameter and the polydispersity index width (PDI width). Three measurements were performed for each sample.

Scanning Electronic Microscopy: The images were collected with a Hitachi SU8000 field-emission scanning electron microscope by setting the accelerating voltage at 3 kV with an emission current of 5 μA.

X-ray Spectromicroscopy: X-ray spectromicroscopy (STXM) measurements were performed on beamline 5.3.2.2 at the ALS synchrotron. Samples were prepared for STXM measurements by spin coating 2.5 mL of nanoparticle ink onto low-stress silicon nitride (Si_3N_4) membrane windows with silicon dioxide coating (window dimensions 0.25 × 0.25 mm^2, window thickness 15 nm, silicon frame dimensions 5 × 5 mm^2, purchased from Norcada, Canada) at 3000 rpm, 1 min, low acceleration of 112 rpm s^{-1}. Full details of the STXM measurement conditions are reported in the previous article, by Barr et al.[32] The radial composition profiles in Figure S2 (Supporting Information) were generated by extracting compositional data from STXM maps imported into MATLAB from aXis2000. The "0" on the x-axis corresponds to the center of the nanoparticle. Note that, since STXM is a transmission technique, the composition measured at the nanoparticle center is the combination of the core plus the shell. More information is available in the article from Holmes et al.[35]

Surface Energy Values: The surface energies referred to P3HT, eh-IDTBR, and o-IDTBR have been taken from the literature.[34] The values represent the surface energies of solids P3HT, eh-IDTBR, and o-IDTBR thin films and have been calculated through contact angle measurements.

Organic Photovoltaic Devices Fabrication: OPV devices were fabricated with an inverted architecture glass/ITO/ZnO/active layer/MoO_3/Ag, where ZnO and MoO_3 were used as electron transport (ETL) and hole transport (HTL) interlayer, respectively. The ITO-covered glasses (1.5 × 1.5 cm^2, 10 Ω/sq, VisionTek) were cleaned by sequential ultrasonic treatments: diluted soap Hellmanex III, deionized water, and isopropanol. The ZnO precursor solution was prepared by mixing zinc acetate dihydrate (165 mg) and ethanolamine (90 μL) with ultrapure ethanol (5 mL). The solution was then stirred at 55 °C in the air for 30 min and left at room temperature under continuous stirring prior to deposition. Before depositing the ETL, the substrates were dried and treated with UV-ozone for 15 min. ZnO precursor solution was then spin-coated to form 40 nm thin films. The substrates were then thermally annealed in air at 180 °C for 30 min. For np-BHJ active layers, substrates were treated with UV-ozone for 20 min before deposition in order to increase the hydrophilicity of the surface. np-BHJ active layers were obtained by spin coating on ZnO-covered substrates of the nanoparticle dispersions with a rotation speed of 2000 rpm (for 230–250 nm). For BHJ active layers deposited from organic solvents, organic solutions were prepared by dissolving 24 mg mL^{-1} of P3HT:o-IDTBR (wt% of 1:1) and P3HT:eh-IDTBR (wt% of 1:1) mixture in chlorobenzene and stirred 2 h at 65 °C in a nitrogen-filled glovebox. Both solutions were spin-coated with a rotation speed of 800 rpm to form the active layer thin film. Subsequently, the active layer was annealed at 100 °C for 10 min. Afterward, for both types of devices (water-processed and organic solvent-processed) vacuum evaporation (P = 10^{-6} mbar) was used to deposit HTL MoO_3 (7 nm thick with a rate of 0.5 Å s^{-1}) and electrode Ag (80 nm thick with a rate of 2 Å s^{-1}). The area of OPV devices was set at 10.5 mm^2.

Current-Voltage Characterization of the Organic Photovoltaic Devices: A solar simulator using a xenon source and AM 1.5 G filters (Newport LCS-100) was used. The light intensity of the lamp was set at 100 mW cm^{-2} using a calibrated silicon reference cell from Newport Co. The *J–V* curves were recorded in the dark and under 1-sun using a Keithley 2400 SMU, and parameters were directly extracted via a LabVIEW program. *J–V* characterization was done in a nitrogen-filled glovebox.

Supporting Information

Supporting Information is available from the Wiley Online Library or from the author.

Acknowledgements

The authors acknowledge the support provided by the ANR through the WATER-PV project N°ANR-20-CE05-0002. The work at LIMMS/CNRS and IIS, University of Tokyo was partly supported by KAKENHI from JSPS (20H05660) as well as the INSIS CNRS and University of Bordeaux in the frame of the BIOMEG project. The authors thank the support from the LIGHT S&T Graduate Program (PIA3 Investment for the Future Program, ANR-17-EURE-0027) for the H.L. travel grant. Y.T. is also supported by the SPRING-GX program and the SEUT program of the University of Tokyo. This research used resources from the Advanced Light Source, which is a DOE Office of Science User Facility under contract no. DE-AC02-05CH11231. The authors thank support staff at the Advanced Light Source synchrotron. The authors acknowledge travel funding provided by the International Synchrotron Access Program (ISAP) managed by the Australian Synchrotron, part of ANSTO, and funded by the Australian Government. This work was performed in part at the Materials Node (Newcastle) of the Australian National Fabrication Facility (ANFF), which is a company established under the National Collaborative Research Infrastructure Strategy to provide nano- and microfabrication facilities for Australia's researchers. The authors thank the University of Newcastle Electron Microscopy and X-ray (EMX) Unit for providing access to electron microscopes. N.P.H. acknowledges the University of Tokyo Institute of Industrial Science (IIS) for funding an IIS Invited International Researcher travel grant. The authors acknowledge Microscopy Australia (ROR: 042mm0k03) at Sydney Microscopy and Microanalysis, University of Sydney, enabled by NCRIS. The authors further thank the support of the University of Sydney Core Research Facilities.

Conflict of Interest

The authors declare no conflict of interest.

Data Availability Statement

The data that support the findings of this study are available from the corresponding author upon reasonable request.

Keywords

charge transport, nanogap, nanojunction, nanoparticles, organic photovoltaic

Received: May 21, 2024
Revised: August 23, 2024
Published online: September 23, 2024

[1] E. K. Solak, E. Irmak, *RSC Adv.* **2023**, *13*, 12244.
[2] S. Wang, H. Zhang, B. Zhang, Z. Xie, W. Y. Wong, *Mater. Sci. Eng. R Reports.* **2020**, *140*, 100547.
[3] J. Chen, W. Zhang, L. Wang, G. Yu, *Adv. Mater.* **2023**, *35*, 2210772.
[4] R. R. Søndergaard, M. Hösel, F. C. Krebs, *J. Polym. Sci., Part B: Polym. Phys.* **2013**, *51*, 16.
[5] G. Bernardo, T. Lopes, D. G. Lidzey, A. Mendes, *Adv. Energy Mater.* **2021**, *11*, 2100342.
[6] T. Shimura, S. Sato, P. Zalar, N. Matsuhisa, *Adv. Electron. Mater.* **2023**, *9*, 2200512.
[7] I. McCulloch, M. Chabinyc, C. Brabec, C. B. Nielsen, S. E. Watkins, *Nat. Mater.* **2023**, *22*, 1304.
[8] F. Torricelli, I. Alessandri, E. Macchia, I. Vassalini, M. Maddaloni, L. Torsi, *Adv. Mater. Technol.* **2022**, *7*, 2100445.
[9] J. Panidi, E. Mazzolini, F. Eisner, Y. Fu, F. Furlan, Z. Qiao, M. Rimmele, Z. Li, X. Lu, J. Nelson, J. R. Durrant, M. Heeney, N. Gasparini, *ACS Energy Lett.* **2023**, *8*, 3038.
[10] D. Ho, J. Lee, S. Park, Y. Park, K. Cho, F. Campana, D. Lanari, A. Facchetti, S. Y. Seo, C. Kim, A. Marrocchi, L. Vaccaro, *J. Mater. Chem. C.* **2020**, *8*, 5786.
[11] J. Cho, K. H. Cheon, J. Ha, D. S. Chung, *Chem. Eng. J.* **2016**, *286*, 122.
[12] C. Ceriani, M. Scagliotti, T. Losi, A. Luzio, S. Mattiello, M. Sassi, N. Pianta, M. Rapisarda, L. Mariucci, M. Caironi, L. Beverina, *Adv. Electron. Mater.* **2023**, 2201160.
[13] A. Holmes, E. Deniau, C. Lartigau-Dagron, A. Bousquet, S. Chambon, N. P. Holmes, *ACS Nano.* **2021**, *15*, 3927.
[14] H. Laval, A. Holmes, M. A. Marcus, B. Watts, G. Bonfante, M. Schmutz, E. Deniau, R. Szymanski, C. Lartigau-Dagron, X. Xu, J. M. Cairney, K. Hirakawa, F. Awai, T. Kubo, G. Wantz, A. Bousquet, N. P. Holmes, S. Chambon, *Adv. Energy Mater.* **2023**, *13*, 2300249.
[15] A. Holmes, H. Laval, M. Guizzardi, V. Maruzzo, G. Folpini, N. Barbero, E. Deniau, M. Schmutz, S. Blanc, A. Petrozza, G. M. Paternò, G. Wantz, S. Chambon, C. Lartigau-Dagron, A. Bousquet, *Energy Environ. Sci.* **2024**, *17*, 1107.
[16] C. Xie, S. Liang, G. Zhang, S. Li, *Polymers (Basel)*. **2022**, *14*, 4229.
[17] M. Bag, T. S. Gehan, D. D. Algaier, F. Liu, G. Nagarjuna, P. M. Lahti, T. P. Russell, D. Venkataraman, *Adv. Mater.* **2013**, *25*, 6411.
[18] J. E. Millstone, D. F. J. Kavulak, C. H. Woo, T. W. Holcombe, E. J. Westling, A. L. Briseno, M. F. Toney, J. M. J. Fréchet, *Langmuir.* **2010**, *26*, 13056.
[19] C. Xie, A. Classen, A. Späth, X. Tang, J. Min, M. Meyer, C. Zhang, N. Li, A. Osvet, R. H. Fink, C. J. Brabec, *Adv. Energy Mater.* **2018**, *8*, 1702857.
[20] C. Xie, X. Tang, M. Berlinghof, S. Langner, S. Chen, A. Späth, N. Li, R. H. Fink, T. Unruh, C. J. Brabec, *ACS Appl. Mater. Interfaces.* **2018**, *10*, 23225.
[21] D. Kim, M. Sonker, A. Ros, *Anal. Chem.* **2019**, *91*, 277.
[22] R. Pethig, *Biomicrofluidics.* **2010**, *4*, 022811.
[23] N. G. Green, H. Morgan, *J. Phys. Chem. B.* **1999**, *103*, 41.
[24] Q. Zhao, W. Wang, J. Shao, X. Li, H. Tian, L. Liu, X. Mei, Y. Ding, B. Lu, *Adv. Mater.* **2016**, *28*, 6337.
[25] R. J. Barsotti, M. D. Vahey, R. Wartena, Y. M. Chiang, J. Voldman, F. Stellacci, *Small.* **2007**, *3*, 488.
[26] M. P. Hughes, K. D. Rosenthal, N. A. Ran, M. Seifrid, G. C. Bazan, T.-Q. Nguyen, *Adv. Funct. Mater.* **2018**, *28*, 1801542.
[27] K. Yim, G. L. Whiting, C. E. Murphy, J. J. M. Halls, J. H. Burroughes, R. H. Friend, J. Kim, *Adv. Mater.* **2008**, *20*, 3319.
[28] P. W. M. Blom, M. J. M. de Jong, J. J. M. Vleggaar, *Appl. Phys. Lett.* **1996**, *68*, 3308.
[29] P. W. M. Blom, V. D. Mihailetchi, L. J. A. Koster, D. E. Markov, *Adv. Mater.* **2007**, *19*, 1551.
[30] K. Yang, Y. Wang, A. Jain, L. Samulson, J. Kumar, *J. Macromol. Sci. Part A.* **2007**, *44*, 1261.
[31] M. Devynck, P. Tardy, G. Wantz, Y. Nicolas, L. Vellutini, C. Labrugère, L. Hirsch, *Appl. Phys. Lett.* **2012**, *100*, 053308.
[32] L. A. Majewski, J. W. Kingsley, C. Balocco, A. M. Song, *Appl. Phys. Lett.* **2006**, *88*, 222108.
[33] A. Zen, J. Pflaum, S. Hirschmann, W. Zhuang, F. Jaiser, U. Asawapirom, J. P. Rabe, U. Scherf, D. Neher, *Adv. Funct. Mater.* **2004**, *14*, 757.
[34] M. G. Barr, S. Chambon, A. Fahy, T. W. Jones, M. A. Marcus, A. L. D. Kilcoyne, P. C. Dastoor, M. J. Griffith, N. P. Holmes, *Mater. Chem. Front.* **2021**, *5*, 2218.
[35] N. P. Holmes, K. B. Burke, P. Sista, M. Barr, H. D. Magurudeniya, M. C. Stefan, A. L. D. Kilcoyne, X. Zhou, P. C. Dastoor, W. J. Belcher, *Sol. Energy Mater. Sol. Cells.* **2013**, *117*, 437.

[36] K. Pei, M. Chen, Z. Zhou, H. Li, P. K. L. Chan, *ACS Appl. Electron. Mater.* **2019**, *1*, 379.
[37] A. F. Paterson, R. Li, A. Markina, L. Tsetseris, S. MacPhee, H. Faber, A.-H. Emwas, J. Panidi, H. Bristow, A. Wadsworth, D. Baran, D. Andrienko, M. Heeney, I. McCulloch, T. D. Anthopoulos, *J. Mater. Chem. C.* **2021**, *9*, 4486.
[38] K. P. Goetz, O. D. Jurchescu, In *Handbook of Organic Materials for Electronic and Photonoic Devices*, 2nd ed., Woodhead Publishing, Sawston, Cambridge **2019**, pp. 453–487.
[39] V. D. Mihailetchi, H. Xie, B. De Boer, L. J. A. Koster, P. W. M. Blom, *Adv. Funct. Mater.* **2006**, *16*, 699.
[40] A. Melianas, V. Pranculis, D. Spoltore, J. Benduhn, O. Inganäs, V. Gulbinas, K. Vandewal, M. Kemerink, *Adv. Energy Mater.* **2017**, *7*, 1700888.
[41] H.-B. Fu, J.-N. Yao, *J. Am. Chem. Soc.* **2001**, *123*, 1434.
[42] K. Vandewal, K. Tvingstedt, A. Gadisa, O. Inganäs, J. V. Manca, *Phys. Rev. B.* **2010**, *81*, 125204.
[43] F. Piersimoni, S. Chambon, K. Vandewal, R. Mens, T. Boonen, A. Gadisa, M. Izquierdo, S. Filippone, B. Ruttens, J. D'Haen, N. Martin, L. Lutsen, D. Vanderzande, P. Adriaensens, J. V. Manca, *J. Phys. Chem. C.* **2011**, *115*, 10873.
[44] K. Vandewal, A. Gadisa, W. D. Oosterbaan, S. Bertho, F. Banishoeib, I. Van Severen, L. Lutsen, T. J. Cleij, D. Vanderzande, J. V. Manca, *Adv. Funct. Mater.* **2008**, *18*, 2064.
[45] Z.-H. Chen, P.-Q. Bi, X.-Y. Yang, M.-S. Niu, K.-N. Zhang, L. Feng, X.-T. Hao, *J. Phys. Chem. C.* **2019**, *123*, 12676.
[46] Q. He, W. Sheng, M. Zhang, G. Xu, P. Zhu, H. Zhang, Z. Yao, F. Gao, F. Liu, X. Liao, Y. Chen, *Adv. Energy Mater.* **2021**, *11*, 2003390.
[47] C. Xie, T. Heumüller, W. Gruber, X. Tang, A. Classen, I. Schuldes, M. Bidwell, A. Späth, R. H. Fink, T. Unruh, I. McCulloch, N. Li, C. J. Brabec, *Nat. Commun.* **2018**, *9*, 5335.
[48] N. P. Holmes, S. Ulum, P. Sista, K. B. Burke, M. G. Wilson, M. C. Stefan, X. Zhou, P. C. Dastoor, W. J. Belcher, *Sol. Energy Mater. Sol. Cells.* **2014**, *128*, 369.

